than the equatorial bond. We also note a change in the pressure evolution of the shortest O–O distance above the transition pressure (Fig. 5B). In the $CaCl_2$ structure, the compression occurs without a further decrease of this short O–O distance, but instead, the O–O first distances evolve toward a comparable value (that is, the oxygen sublattice becomes more symmetrical).

The modification of the a and b cell parameters above 54 GPa is achieved by a rapid rotation of the SiO_6 octahedra in the (a, b) plane, as supported by the pressure evolution of the (x, y, 0) oxygen coordinates (Table 4). The octahedral volumes are calculated from the set of SiO bond lengths. The octahedral bulk moduli, with single-crystal data (*20*) and pressures below 53.2 GPa or above 63 GPa were found to be significantly different in stishovite and $CaCl_2$ forms of SiO_2 (Table 3). Our results are compatible with an integrated octahedral volume variation of about +1% between stishovite and $CaCl_2$-type SiO_2 above the transition pressure (this integrated volume is a volume excess that is built across the second-order phase transformation). This volume variation does not affect the unit cell volume because other structural entities compensate for this volume excess. This suggests that, in stishovite, the SiO_6 compression is high and that the octahedral volume relaxes in the $CaCl_2$ form of SiO_2. We thus propose that, when it adopts the *mmm* point group, the ideal SiO_6 octahedral K_0 is that calculated for the $CaCl_2$ form of SiO_2 (K_0 = 311 ± 1; K' = 4.95 ± 0.05).

The integrated 1% volume variation of SiO_6 octahedra (ΔV_{octa}) corresponds to a compression work of ~35 kJ ($P\Delta V_{octa}$), which is much higher than the maximal integrated energy variation that is involved in the transition of <1.5 kJ/mol. This suggests an energy exchange between SiO_6 octahedra and other polyhedra of the lattice during the phase transition. A similar redistribution could also affect thermal energy. For example, with the entropy change that is related to the pressure evolution of the (a – b)/a–order parameter, there might be an entropy gain that is related to the achievement of a more symmetrical oxygen sublattice (Fig. 5B).

We observed a continuous increase of the SiO_2 density up to the pressures of Earth's CMB (Fig. 4). We coupled this EOS (Table 3) with those that were previously reported in similar experimental conditions for $MgSiO_3$ (V_0 = 162.6 Å^3, K_0 = 256 GPa, and K' = 4) (*17*) and MgO (V_0 = 74.70 Å^3, K_0 = 167 GPa, and K' = 4.5) (*15*). We calculated that the ΔV value that is related to the $MgSiO_3 \rightarrow MgO + SiO_2$ breakdown reaction is positive at all pressures. At 300 K, ΔV increases from ~1 to 4% of the perovskite volume between 25 and 120 GPa, respectively. It might be argued that high-temperature conditions or minor elements can reverse this sign, but so far no such inversion has been observed in high-pressure experiments. Therefore, silicate perovskite is denser than a mixture of its oxides down to the CMB. Consequently, the proposal that free silica could occur in Earth's lower mantle is not supported by the present data, so lor[illegible] an excess of magnesiowüstite (Mg,Fe)O is thought to be present in the lower mantle.

References and Notes

1. J. Haines, J.-M. Léger, O. Schulte, *J. Phys. Condens. Matter* **8**, 1631 (1996).
2. At the CMB, pressure and temperature are 135 GPa and between 3000 and 4000 K, respectively. Experimental results suggested that $MgSiO_3$ breaks down into MgO periclase and SiO_2 above 58 GPa [S. K. Saxena *et al.*, *Science* **274**, 1357 (1996)].
3. Y. Tsuchida and T. Yagi, *Nature* **340**, 217 (1989).
4. J. K. Kingma, H. K. Mao, R. J. Hemley, *High Pressure Res.* **14**, 363 (1996).
5. J. K. Kingma, R. E. Cohen, R. J. Hemley, H. K. Mao, *Nature* **374**, 243 (1995).
6. R. E. Cohen, in *High-Pressure Research: Application to Earth and Planetary Sciences*, vol. 67 of *Geophysical Monograph Series*, Y. Syono and M. H. Manghnani, Eds. (American Geophysical Union, Washington, DC, 1992), pp. 425–431.
7. B. B. Karki, M. C. Warren, L. Stixrude, G. J. Ackland, J. Crain, *Phys. Rev. B* **55**, 3465 (1997).
8. J. S. Tse, D. D. Klug, Y. Le Page, *Phys. Rev. Lett.* **69**, 3647 (1992).
9. D. J. Lacks and R. G. Gordon, *J. Geophys. Res.* **98**, 22147 (1993).
10. A. El Goresy, L. Dubrovinsky, S. Saxena, T. G. Sharp, *Meteoritics* **33** (suppl.), A45 (1998).
11. L. G. Liu, *Earth Planet. Sci. Lett.* **49**, 166 (1980).
12. J. Haines, J. M. Léger, O. Schulte, *Science* **271**, 629 (1996).
13. J. C. Jamieson, J. N. Fritz, M. H. Manghnani, in *High-Pressure Research in Geophysics*, Y. Akimoto and M. H. Manghnani, Eds. (Reidel, Boston, MA, 1982), pp. 425–431.
14. J. Haines, J.-M. Léger, S. Hoyau, *J. Phys. Chem. Solids* **56**, 965 (1995).
15. G. Fiquet, D. Andrault, J.-P. Itié, P. Gillet, P. Richet, *Phys. Earth Planet. Inter.* **95**, 1 (1996).
16. D. Andrault, G. Fiquet, M. Kunz, F. Visocekas, D. Häusermann, *Science* **278**, 831 (1997).
17. G. Fiquet *et al.*, *Phys. Earth Planet. Inter.* **105**, 21 (1998).
18. J. Hammersley, *Publication No. ESRF98HA01T* (ESRF, Grenoble, France, 1996).
19. A. C. Larson and R. B. Von Dreele, *GSAS Manual* (Los Alamos National Laboratory, Los Alamos, NM, 1994), pp. 86–748; A. LeBail, in *Accuracy in Powder Diffraction*, E. Prince and J. K. Stalick, Eds. (National Institute of Standards and Technology, Gaithersburg, MD, 1992), p. 213.
20. N. L. Ross, J. F. Shu, R. M. Hazen, T. Gasparik, *Am. Mineral.* **75**, 739 (1990).
21. R. J. Hemley, C. T. Prewitt, K. J. Kingma, in *Silica: Physical Behavior, Geochemistry and Materials Applications*, P. J. Heaney, C. T. Prewitt, G. V. Gibbs, Eds. (Mineralogical Society of America, Washington, DC, 1994), pp. 41–81.
22. R. E. Cohen, *Am. Mineral.* **76**, 733 (1991).
23. E. K. H. Salje, *Phase Transitions in Ferroelastic and Co-Elastic Crystals* (Cambridge Univ. Press, New York, 1990).
24. F. Guyot, P. Richet, P. Courtial, P. Gillet, *Phys. Chem. Miner.* **20**, 141 (1993); D. de Ligny and P. Richet, *Phys. Rev. B* **53**, 3013 (1996).
25. D. J. Weidner, J. D. Bass, A. E. Ringwood, W. Sinclair, *J. Geophys. Res.* **87**, 4740 (1982).

26. We thank T. Charpin, P. Richet, N. L. Ross, and two anonymous referees for their help and comments. D.A. thanks M. Kunz and L. W. Finger for their help with the GSAS code. This work was supported by the CNRS Institut National des Sciences de l'Univers, Institut de Physique du Globe, and ESRF programs.

7 July 1998; accepted 16 September 1998

Thermodynamics of Calcite Growth: Baseline for Understanding Biomineral Formation

H. Henry Teng, Patricia M. Dove,* Christine A. Orme, James J. De Yoreo

The complexity of biomineralized structures suggests the potential of organic constituents for controlling energetic factors during crystal synthesis. Atomic force microscopy was used to investigate the thermodynamic controls on carbonate growth and to measure the dependence of step speed on step length and the dependence of critical step length on supersaturation in precisely controlled solutions. These data were used to test the classic Gibbs-Thomson relationship and provided the step edge free energies and free energy barriers to one-dimension nucleation for calcite. Addition of aspartic acid, a common component in biomineralizing systems, dramatically affected growth morphology and altered the magnitude of the surface energy.

Many organisms mediate inorganic crystallization by selective application of organic compounds (*1*–*3*) to exert detailed control over the structure (*3*), orientation (*1*), growth kinetics (*2*), and nucleation sites (*4*) of inorganic crystals. An understanding of physical controls on biomineralization promises new routes to the controlled synthesis of complex crystalline structures for application across a broad spectrum of materials-based technologies. Because it occurs ubiquitously among biomineralizing systems (*5*) and it is easily crystallized, calcite—often in combination with aspartic acid–rich protein mixtures (*1*, *2*,

5)—has emerged as a model crystal for developing this understanding (*3, 6–8*). Here we use in situ force microscopy (AFM) to quantify the fundamental energetic and kinetic parameters of calcite growth and the effect of organic molecules on those parameters in pure and aspartic acid–bearing solutions.

We examined calcite crystallization from solution onto a seed crystal according to established methods (*9, 10*). We carefully controlled solution chemistry with ionic strength fixed at 0.11 M, pH adjusted to 8.50, and the ratio of calcium to carbonate activity held at 1.04. The pCO_2 was fixed by using a closed-system configuration. Calcium and carbonate activities were determined from the Davies equation (*11*). In situ AFM imaging at 25°C was performed in Contact Mode (Digital Instruments, Santa Barbara) by continuously flowing supersaturated solutions through the fluid cell at rates so that step velocity was independent of flow rate, ensuring that growth was not limited by mass transport to the surface. The birth of new steps at dislocations was monitored and the lengths of these steps were measured immediately before and after they began to advance. The critical length, L_c, was taken as the average of these lengths (*10*). Step velocity was estimated by reference to a fixed point (the dislocation source) or by changes in the apparent step orientation (*10*).

The supersaturation, σ, is defined by (*11*)

$$\sigma \equiv \Delta\mu/k_bT \quad (1a)$$

$$= \ln(a/a_e) \quad (1b)$$

or for $CaCO_3$ in an aqueous solution

$$\sigma = \ln[a(Ca^{2+})a(CO_3^{2-})/K_{sp} \quad (1c)$$

where $\Delta\mu$ is change in chemical potential per molecule, k_b is the Boltzmann constant, T is absolute temperature, a and a_e are actual and equilibrium activity products, K_{sp} is the equilibrium solubility at zero ionic strength, and $a(i)$ is the activity of the ith species. K_{sp} ($10^{-8.54}$) was calculated from the activity at which measured step speeds went to zero (*12*).

We present results for σ = 0.04 to 1.4. In this range, layer growth of calcite occurred on $\{10\bar{1}4\}$ by advancement of 3.1 Å monomolecular steps generated at dislocations and separated by atomically flat terraces (Fig. 1, A and B). Step advancement led to the formation of polygonal growth hillocks with steps parallel to $\langle\bar{4}41\rangle$ directions. Step geometry is shown in Fig. 1, C and D. The *c*-glide symmetry plane generated two distinct pairs of crystallographically identical steps denoted as the positive ($[\bar{4}41]_+$ and $[48\bar{1}]_+$) and negative ($[\bar{4}41]_-$ and $[48\bar{1}]_-$) directions (*13*).

The structure of the growth hillock depends on the thermodynamics of step advancement through terrace widths $T_\pm$ and step speeds $v_\pm$, which are related by $T_+/T_- = v_+/v_-$. The growth rate of the crystal normal to the surface, R, is determined by these parameters through $R = h\,v_\pm/T_\pm$, where h is step height. The $v_\pm$ is determined by the attachment and detachment kinetics at kink sites and differs for the two step types because of the nonequivalence in kink site structure (*9, 13*). In contrast, $T_\pm$ should be determined by the equilibrium thermodynamics of the step edges through the Gibbs-Thomson effect (*14*). Consider the birth of a new spiral segment (Fig. 1, A and B). If it remains in equilibrium with the adjacent reservoir of growth units, then it will advance only when the change in free energy, Δg, associated with the

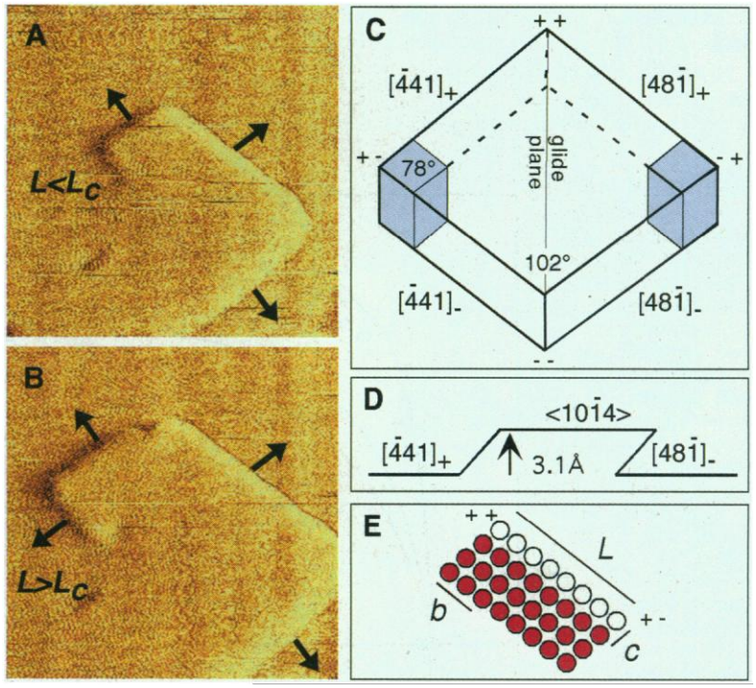

Fig. 1. (**A** and **B**) AFM images (1 × 1 μm) of growth hillocks on $\{10\bar{1}4\}$ face of calcite showing development of a new spiral segment. Arrows indicate advancing step segments. (**C**) Schematic of calcite $\{10\bar{1}4\}$ terrace illustrating anisotropy. (**D**) Cross section of $\{10\bar{1}4\}$ terrace showing step geometry. (**E**) Plan view of edge showing relationship of length to lattice parameters.

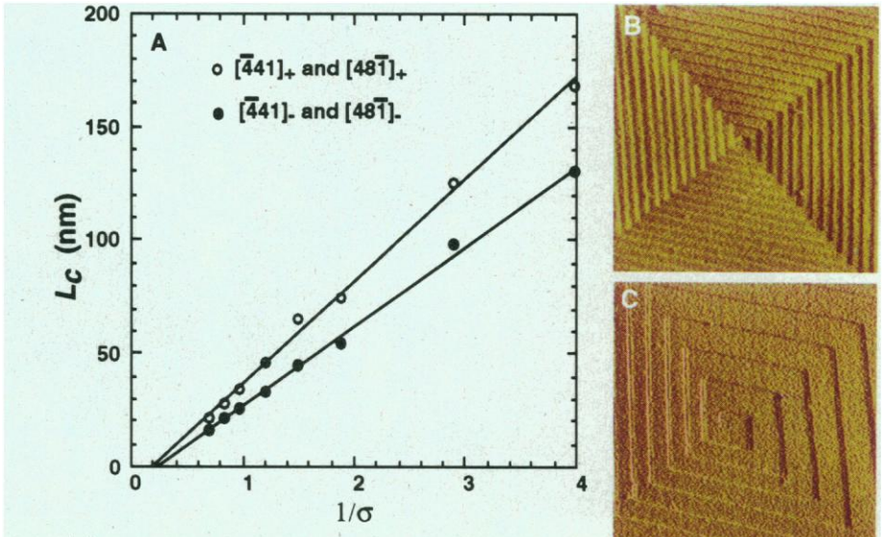

Fig. 2. (**A**) Dependence of critical length on supersaturation along with images (5 × 5 μm) showing effect of L_c on $T_\pm$. (**B**) High σ, short L_c; (**C**) low σ, long L_c.

H. H. Teng and P. M. Dove, School of Earth and Atmospheric Sciences, Georgia Institute of Technology, Atlanta, GA 30332, USA. C. A. Orme and J. J. De Yoreo, Department of Chemistry and Materials Science, Lawrence Livermore National Laboratory, Livermore, CA 94550, USA.

*To whom correspondence should be addressed. E-mail: dove@eas.gatech.edu

addition of a new row of growth units is negative. Taking into account the anisotropy in calcite step structure, one can show that Δg for a straight step is

$$\Delta g_{\pm} = -(L/b)\Delta\mu + 2c\langle\gamma\rangle_{\pm} \quad (2a)$$

$$\langle\gamma\rangle_{+} = (1/4)[2(\gamma_{+} + \gamma_{-}) + (\gamma_{++} + \gamma_{+-})] \quad (2b)$$

$$\langle\gamma\rangle_{-} = (1/4)[2(\gamma_{+} + \gamma_{-}) + (\gamma_{--} + \gamma_{+-})] \quad (2c)$$

where L is the length of the step, b is the 6.4 Å intermolecular distance along the step, c is the 3.2 Å distance between rows, γ_{+} and γ_{-} are the step edge free energies along the + and − steps, and γ_{++}, γ_{--}, and γ_{+-} are contributions to the step edge free energy from the corner sites (Fig. 1, C and E). When step curvature is included, the second term on the right-hand side of Eq. 2a becomes an integral of $\langle\gamma\rangle_{\pm}$ over the step segment as a function of step orientation. Setting Δg to zero and substituting Eq. 1a into Eq. 2a shows that steps advance only if L exceeds a critical value, L_c, given by

$$L_{c\pm} = 2bc\langle\gamma\rangle_{\pm}/k_bT\sigma \quad (3)$$

Alternatively, setting $\Delta g = 0$ for a step of arbitrary length gives the length-dependent equilibrium activity, $a_e(L)$

$$a_e(L) = a_{e,\infty}\exp(2bc\langle\gamma\rangle/Lk_bT) \quad (4a)$$

$$= a_{e,\infty}\exp(\sigma L_c/L) \quad (4b)$$

where subscript ∞ refers to the infinitely long step and a and $a_{e,\infty}$ are related by $a = i_{e,\infty}\exp(\sigma)$. Equations 4a and 4b are statements of the Gibbs-Thomson effect (*14*), which predicts that L_c should scale inversely with σ as in Eq. 3.

In agreement with Eq. 3, we observed that the measured L_c varied inversely with σ for the two step directions on the calcite $\{10\bar{1}4\}$ faces (Fig. 2). The slope of the relationship between L_c and $1/\sigma$ for both types of steps gives values of $\langle\gamma\rangle_{+} = 2.75$ and $\langle\gamma\rangle_{-} = 2.15$ eV/nm. From Eqs. 2b and 2c, it follows that the difference between $\langle\gamma\rangle_{+}$ and $\langle\gamma\rangle_{-}$ associated with the ++ and −− corners is about 0.77 eV per molecule.

These measurements provide a direct test

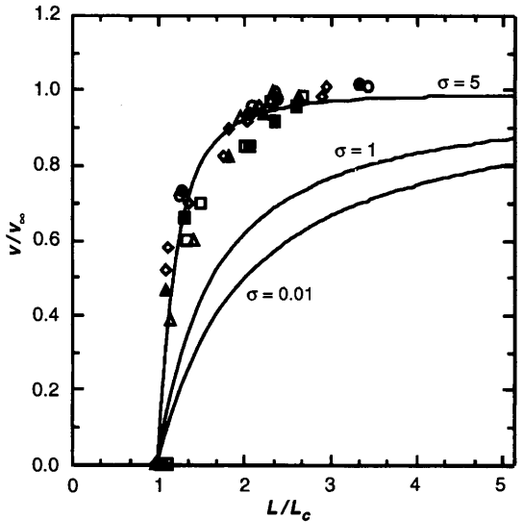

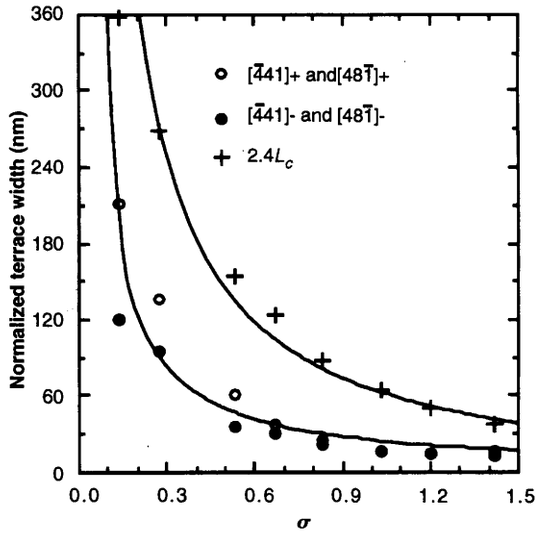

Fig. 3. (Left) Dependence of step speed on step length. Symbols give data points for $[441]_{-}$ and $[48\bar{1}]_{-}$ steps (open symbols) and $[\bar{4}41]_{+}$ and $[48\bar{1}]_{+}$ steps (closed symbols), with $\sigma = 0.826$ (triangles), 0.668 (squares), 0.534 (diamonds), and 0.346 (circles). Solid lines are obtained from Eq. 6. **Fig. 4. (Right)** Measured dependence of normalized terrace widths, $\{\sin\theta/[2(1 + B)]\}T_{+}$ and $\{\sin\theta/[2(1 + 1/B)]\}T_{-}$, on σ. Predicted value of normalized width expected from classic growth models, $2.4\langle L_c\rangle$, is given by crosses. Symbols give data for $[\bar{4}41]_{-}$ and $[48\bar{1}]_{-}$ steps (closed symbols) and $[\bar{4}41]_{+}$ and $[48\bar{1}]_{+}$ steps (open symbols). Solid lines are $1/\sigma$ fits to data.

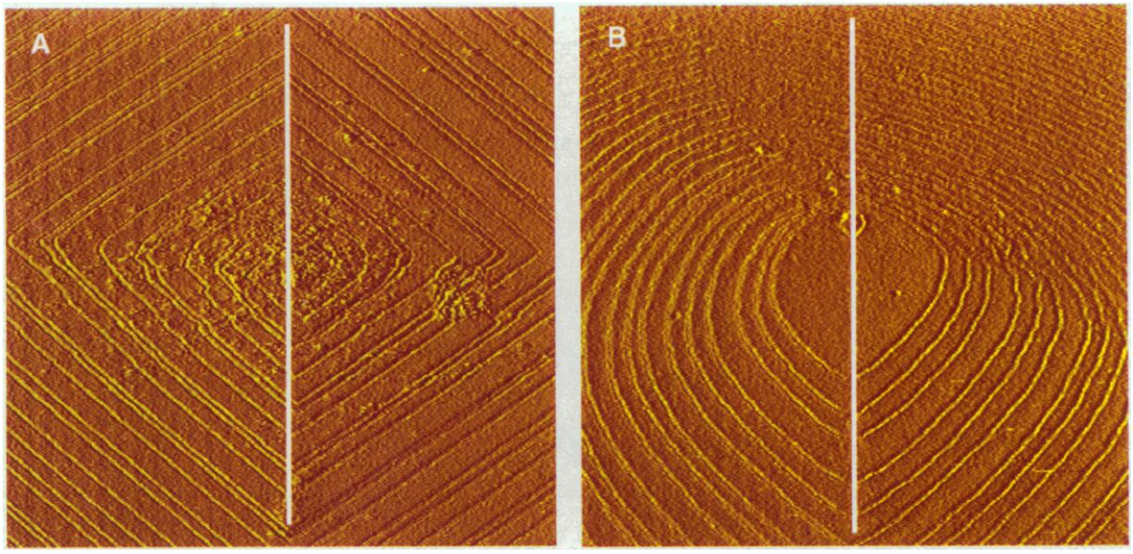

Fig. 5. AFM images (9 × 9 μm) showing effect of aspartic acid on growth hillock morphology before (**A**) and after (**B**) addition. Solid vertical lines show location of glide plane.

of the Gibbs-Thomson effect on crystal growth in any system and show that steps on calcite behave in accordance with equilibrium thermodynamics. This conclusion has implications for understanding the role of kinetics in controlling step advancement. Because the local atomic configurations at kink sites control the attachment and detachment kinetics, sites far from the corners should exhibit dynamics that are independent of step length. When $\sigma > 1$, then, even on a subcritical step, attachment to these sites will always be more rapid than detachment. Thus for the step to behave in accordance with Eq. 3, equilibrium with the surrounding thermodynamic reservoir must be maintained by the sites of high curvature near corners where detachment is preferred, and sites along the step must communicate with the near-corner sites on a time scale that is short compared with the time required to add on another row. These results imply that transport along the steps, whether by edge, surface, or bulk diffusion, is rapid enough to keep steps in equilibrium with the adjacent fluid.

The dependence of $L_{c\pm}$ versus $1/\sigma$ exhibits a nonzero intercept that marks the supersaturation $\sigma_{r\pm}$, where $L_{c\pm}$ goes to zero (Fig. 2). For $\sigma > \sigma_{r\pm}$, one-dimensional nucleation occurs along the step edges, and the steps become kinetically roughened. This supersaturation gives the approximate free energy barrier, $g_{1D\pm}$, to the formation of a stable dimer on step edges (*15*) through $g_{1D\pm} = kT\sigma_{r\pm}$. From the measured intercepts we obtain values for $g_{1D\pm}$ of 0.14 and 0.10 eV, respectively.

When the steps are long (>500 nm), the dependence of v on saturation state in the absence of impurity effects is given by (*9*)

$$v = \omega\beta[a(Ca^{2+}) - a_e(Ca^{2+})] \quad (5)$$

where ω is the volume per growth unit in the solid and β is the kinetic coefficient (*16*). Combining Eqs. 1, 4, and 5 leads to a length-dependent step speed

$$v_{\pm}(L) = v_{\pm,\infty}\{1 - [e^{(\sigma r L_{c\pm}/L)} - 1]/[e^{\sigma} - 1]\} \quad (6)$$

where $v_{\pm,\infty}$ is given by Eq. 5 for $a_c(L \rightarrow \infty)$. [When $\sigma << 1$, Eq. 6 reduces to a commonly used approximation: $v = v_{\infty}(1 - L_c/L)$ (*17*).] The measured speed is independent of σ or step direction and rises much more rapidly than that predicted by Eq. 6 (Fig. 3).

Equation 6 was originally derived for spirals with isotropic step edge energies and kinetics and assumes a high kink site density so that the rate of attachment is not limited by the availability of kinks. Voronkov (*18*) proposed that, for highly polygonalized spirals, the distance between kink sites along a step is large so that the attachment rate is limited by their availability. He pointed out that the equilibrium shape of a step should be curved toward the corners and that the straight, central portion—which determines the speed—comprises only a small fraction of the step. (This prediction of step shape is verified in Fig. 1, A and B.) When the neighboring step advances, there is a rapid increase in the relative size of the straight portion and hence in the number of available kink sites. As a result, when L exceeds L_c, the step speed rises rapidly to its limiting value as its length increases from L_c to L', whose order of magnitude is given by $L_c + 2\omega/hc\sigma$. Substituting in the values of ω, h, and c for calcite, we obtain $L'/L_c \sim 1.1$, a prediction that is consistent with the results (Fig. 3).

This rapid rise of $v(L)$ affects the magnitude of $T_{\pm}$ and hence R. Consider an isotropic square spiral. If v rose discontinuously from zero at $L < L_c$ to v_{∞} at $L > L_c$, then $T_{\pm}$ would equal $4L_c$ (*17*). However, because v rises gradually from zero to v_{∞}, $T_{\pm}$ is larger by a factor that we refer to as the Gibbs factor, G. The Gibbs-Thomson prediction (Eq. 6) leads to $G = 2.4$ for small σ—giving $T_{\pm} = 9.6L_{c\pm}$ (*17*). As σ increases, G decreases to 1.0 in the limit of large σ.

To compare these predictions with our results for calcite, we must account for the anisotropy of the rhombohedral spiral on $\{10\bar{1}4\}$ faces. The terrace widths for the two step directions become

$$T_{+} = 2G(1 + B)\langle L_c\rangle/\sin\theta \quad (7a)$$

$$T_{-} = 2G(1 + 1/B)\langle L_c\rangle/\sin\theta \quad (7b)$$

where B is v_{+}/v_{-}, $\langle L_c\rangle$ is the average value of L_c for the two step directions, and θ is the angle between adjacent turns of the spiral. Figure 4 shows the measured dependence of $T_{\pm}$ on σ as well as $T_{\pm} = 2.4\langle L_c\rangle$ obtained by using Eq. 6 at small σ. As predicted, $T_{\pm}$ scales inversely with σ, but because of the anomalously rapid rise in $v(L)$, the measured G factor is close to one. Consequently, the growth rate, R, of the calcite surface is about 2.5 times that predicted from classic theory (*14, 17*).

These results on pure calcite provide a firm basis for quantifying how biomolecules mediate mineralization. Addition of aspartic acid to growth solutions has a dramatic effect on spiral morphology (Fig. 5). While negative steps are still present, the glide plane no longer defines a line of symmetry. The hillock becomes asymmetric, exhibiting new step directions, terrace widths, and highly rounded step corners. Some of these morphological changes such as step rounding are due in part to kinetic factors, but each of these features demonstrates the importance of surface energetic controls. Most importantly, the presence of new equilibrium step directions shows that the low-energy facets as determined from the Wulff construction have changed. In addition, the much smaller terrace widths associated with these new steps demonstrate lower step edge free energy. We estimate the new step edge energy to be only ~1 eV per molecule, smaller than for steps on pure calcite by a factor of about three.

The most plausible explanation for this behavior is that aspartic acid forms an ordered adsorption layer on the facets defined by the new step directions, thereby lowering the surface free energy through a change in the equilibrium activity of solutions contacting those facets. This behavior is documented for other systems such as NaCl, where a variety of compounds form ordered adsorption layers (*19*). These layers act as surfactants, lowering the surface free energy and stabilizing facets unexpressed in the pure system. The most notable of these compounds is glycine, which, like aspartic acid, possesses a terminal carboxyl group that binds to both Na and Ca and causes expression of {120} faces on NaCl (*19*). Thus it appears that the primary effect of aspartic acid on calcite crystallization is to alter the equilibrium thermodynamics of the growth surface.

References and Notes

1. A. Berman, L. Addadi, S. Weiner, *Nature* **331**, 546 (1988).
2. S. Mann *et al.*, *Science* **261**, 1286 (1993).
3. A. M. Belcher, X. H. Wu, R. J. Christensen, P. K. Hansma, *Nature* **381**, 56 (1996).
4. A. Winter and S. G. Seisser, Eds., *Coccolithophores* (Cambridge Univ. Press, New York, 1994).
5. S. Mann, *Nature* **365**, 499 (1993).
6. H. H. Teng and P. M. Dove, *Am. Mineral.* **82**, 878 (1997).
7. D. A. Walters *et al.*, *Biophys. J.* **72**, 1425 (1997).
8. C. S. Sikes, M. L. Yeung, A. P. Wheeler, in *Surface Reactive Peptides and Polymers: Discovery and Commercialization*, C. S. Sikes and A. P. Wheeler, Eds. (ACS Books, Washington, DC, 1991), pp. 50–71.
9. H. H. Teng, P. M. Dove, J. J. De Yoreo, unpublished data.
10. T. A. Land, J. J. De Yoreo, J. D. Lee, *Surf. Sci.* **384**, 136 (1997).
11. J. I. Drever, *The Geochemistry of Natural Waters* (Prentice Hall, Upper Saddle River, NJ, ed. 3, 1997).
12. The most widely reported K_{sp} values range from $10^{-8.36}$ to $10^{-8.29}$ [see (*20*) and references therein]. Because steps on $\{10\bar{1}4\}$ faces migrate at measurable rates when the ionic activity product (IAP) of our solution was equal to the lowest reported value, we determined K_{sp} from IAP measurements where step velocity equaled zero. This lower solubility is due to the lower pCO_2 of our closed experimental system.
13. J. Paquette and R. J. Reeder, *Geochim. Cosmochim. Acta* **59**, 735 (1995).
14. W. K. Burton, N. Carbrera, F. C. Frank, *Philos. Trans. R. Soc. London Ser. A* **243**, 299 (1951).
15. A. A. Chernov, in *Materials Science Forum, Vols. 276–277: Theoretical and Technological Aspects of Crystal Growth*, R. Fornari and C. Paorichi, Eds. (TransTech Publications, Aedermannsdorf, 1998), pp. 71–78.
16. A. A. Chernov and H. Komatsu, in *Science and Technology of Crystal Growth*, J. P. van der Eerden and O. S. L. Bruinsma, Eds. (Kluwer Academic, Dordrecht, Netherlands, 1995), pp. 67–80.
17. L. N. Rashkovich, *KDP Family Single Crystals* (Hilger, New York, 1991).
18. V. V. Voronkov, *Sov. Phys. Crystallogr.* **18**, 19 (1973).
19. R. Kern, in *The Growth of Crystals*, N. N. Sheftal, Ed. (Consultants Bureau, New York, 1969), pp. 3–23.
20. A. Mucci, *Am. J. Sci.* **283**, 780 (1983).

21. We thank S. Potapenko for discussions. This work was performed under the auspices of the U.S. Department of Energy, Division of Geosciences and Engineering, by Georgia Institute of Technology (DE-FG02-98ER14843) and Lawrence Livermore National Laboratory under contract W-7405-Eng-48.

23 July 1998; accepted 21 September 1998